Terahertz-based longitudinal phase space diagnostics of laser wakefield accelerated electron beams

Zhihao Chen, Yu Fang, Ran Li, Xiancong Yang, Tianliang Zhang, and Jianfei Hua*
Department of Engineering Physics, Tsinghua University, Beijing 100084, China

Fei Li
Institute of High Energy Physics, Chinese Academy of Sciences, Beijing 100049, China

Wei Lu
Institute of High Energy Physics, Chinese Academy of Sciences, Beijing 100049, China and Beijing Academy of Quantum Information Sciences, Beijing 100193, China

(Dated: August 11, 2026)

Femtosecond relativistic electron beams are key probes of ultrafast dynamics, and their pulse duration directly limits the achievable temporal resolution. Laser wakefield acceleration (LWFA) provides a compact source of such beams, but the injection-induced energy spread makes bunch compression sensitive to nonlinear longitudinal transport, motivating direct longitudinal phase space (LPS) measurements. Here, a terahertz transverse-deflecting cavity (THz-TDC) combined with a dipole magnet is used to reconstruct the nonlinear LPS of LWFA electron bunches compressed in a double-bend achromat (DBA), resolving a characteristic C-shaped distribution associated with higher-order longitudinal transport. At an average energy of approximately 4.55 MeV, the diagnostic achieves a temporal resolving power of 1.8 fs and an energy resolution of 6.0 keV, corresponding to a relative energy resolution of 0.13%. For comparable energy spreads of approximately 2.9%, shifting the transmitted energy-window center from 4.574 MeV to 4.532 MeV moves the selected beam away from a low-slope region of the nonlinear LPS and increases the root-mean-square bunch length from 26 fs to 42 fs; with the window center held near 4.553 MeV, increasing the energy spread from 2.0% to 4.4% lengthens the bunch from 27 fs to 44 fs. These results show that the final bunch duration is governed by both the position and width of the transmitted energy window within the nonlinear LPS, establishing an LPS-guided strategy for optimizing DBA-compressed LWFA electron bunches and providing a basis for future higher-order phase-space correction.

arXiv:2608.08586v1 [physics.acc-ph] 9 Aug 2026

I. INTRODUCTION

Relativistic electron beams with femtosecond-scale durations are important probes for resolving transient processes at microscopic scales, with applications ranging from ultrafast electron diffraction (UED) [1–4] and microscopy (UEM) [5, 6] to broader ultrafast electron-based imaging of transient electromagnetic structures, such as plasma wakefields [7, 8]. In these applications, the electron pulse duration is a key factor determining the achievable temporal resolution, making ultrashort bunch generation and compression essential. Laser wakefield acceleration (LWFA) has emerged as a promising compact approach, as the small-scale plasma accelerating structure intrinsically enables the generation of femtosecond-scale electron bunches [9–11]. However, the finite energy spread introduced during injection makes these bunches particularly sensitive to energy-dependent longitudinal transport during subsequent propagation [12, 13]. In a drift section, electrons with different energies accumulate different time of flight, leading to temporal broadening. This longitudinal dispersion is characterized by the first-order transport coefficient, $R_{56} = L/\gamma^2$, where L is the drift length and γ represents the relativistic Lorentz factor. This effect is non-negligible for few-MeV electron beams, where the velocity remains sufficiently energy-dependent that, for example, a 1% energy spread over a meter-scale propagation distance can increase an initially few-femtosecond bunch duration to hundreds of femtoseconds.

To mitigate this temporal elongation, beamlines often employ bunch compression schemes, among which magnetic compression is one of the most widely used approaches. Magnetic compression utilizes dispersive sections, such as chicanes [14–16], α-magnets [17–20], and double-bend achromats (DBAs) [21–23], to introduce energy-dependent path lengths for electrons with different energies. The resulting longitudinal delay can compensate the velocity-induced temporal broadening accumulated during beam propagation. In terms of the first-order longitudinal transport, the compensation condition can be expressed as

$$R_{56} = R_{56,\mathrm{prop}} + R_{56,\mathrm{comp}} \approx 0, \tag{1}$$

where $R_{56,\mathrm{prop}}$ represents the longitudinal dispersion accumulated during beam propagation, and $R_{56,\mathrm{comp}}$ denotes the compensating contribution introduced by the magnetic compression section. However, as this first-order term is tuned toward zero, second-order effects become increasingly important, and the linear compression picture is no longer sufficient to describe the beam dy-

* jfhua@tsinghua.edu.cn

namics. To second order, the longitudinal coordinate can be written as $z = z_0 + R_{56}\delta_0 + T_{566}\delta_0^2$ [11], where z_0 and z denote the longitudinal coordinates before and after transport, δ_0 is the initial relative energy deviation, and T_{566} is the second-order longitudinal transport coefficient. The T_{566} term bends an initially quasi-linear time–energy correlation into a nonlinear longitudinal phase space (LPS). Equivalently, the local time–energy slope is given by

$$\frac{\partial z}{\partial \delta_0} = R_{56} + 2T_{566}\delta_0. \tag{2}$$

This relation shows that different energy regions of a nonlinear LPS can have different temporal projections, and that a broader energy spread covers a wider range of nonlinear phase space. Consequently, the final bunch duration depends not only on the energy spread, but also on the position of the energy range relative to a region with a small local time–energy slope.

For LWFA beams, the broad occupied energy range can make the second-order contribution $T_{566}\delta_0^2$ appreciable across the bunch, leading to pronounced nonlinear LPS distortions. Directly resolving the LPS is therefore essential not only for identifying the nonlinear time—energy correlation, but also for determining how the accessible energy range should be selected to optimize the final bunch duration.

Longitudinal phase-space diagnostics have been widely developed in conventional accelerator beamlines to characterize and optimize ultrashort electron bunches. Transverse deflecting structures combined with dispersive sections can directly map the temporal and energy coordinates of the bunch onto a transverse screen, enabling measurements of the current profile, energy chirp, slice energy spread, and two-dimensional LPS [24, 25]. Tomographic and wakefield-based approaches have also been used to reconstruct or infer the LPS [26–28]. In parallel, higher-order phase-space manipulation using sextupole magnets, harmonic radio-frequency fields, and plasma-based linearizers has been explored to compensate nonlinear longitudinal transport or energy chirp [29–32]. These studies establish the importance of LPS-resolved diagnostics for compression tuning and nonlinear correction. Most previous work, however, has focused on conventional accelerator beams, global compression settings, or dedicated linearization elements. For LWFA beams with an injection-induced broad energy spread, it remains less explored how a directly measured nonlinear LPS can be used to select the transmitted energy range and optimize the final bunch duration when first- and second-order longitudinal transport act simultaneously.

For femtosecond-scale electron beams, a terahertz transverse deflecting cavity (THz-TDC) provides a compact approach to LPS reconstruction with femtosecond-level temporal resolving power [19, 33–35]. In this work, a THz-TDC combined with a dipole magnet is employed to experimentally reconstruct the nonlinear LPS of LWFA electron bunches during double-bend-achromat (DBA)-based compression. The measurement directly resolves a characteristic C-shaped LPS induced by higher-order longitudinal transport. More importantly, rather than using the reconstructed LPS only to characterize the compression state, the measured nonlinear LPS provides an operational guide for aperture-defined energy-window control in the DBA. By varying both the central energy and the transmitted energy spread, different local-slope regions of the nonlinear LPS are selected, allowing the final bunch duration to be optimized under the combined influence of first- and second-order longitudinal transport. Space-charge-inclusive simulations reproduce the nonlinear LPS evolution and its energy-window-dependent bunch-duration behavior. The present work therefore advances LPS diagnostics from post-compression characterization to an experimentally accessible optimization strategy for compact LWFA beamlines, while also providing direct guidance for future higher-order LPS linearization.

The remainder of this paper is organized as follows. Section II introduces the DBA-based compression principle and the role of energy-window tuning, followed by numerical simulations of nonlinear LPS evolution and bunch-length optimization. Section III describes the experimental implementation of the THz-TDC diagnostic system, including THz pulse characterization, temporal and energy resolution calibration, and LPS reconstruction under different energy-window conditions. Section IV summarizes the main results and discusses their implications for optimizing electron-bunch compression in LWFA-UED beamlines.

II. NUMERICAL SIMULATION OF DBA-BASED NONLINEAR LPS EVOLUTION

A. Principle of DBA-Based Compression

The DBA section provides magnetic bunch compression by introducing energy-dependent longitudinal transport. In the dipoles, electrons with different energies follow different trajectories and therefore acquire different effective path lengths. This DBA-induced path-length difference generates a longitudinal delay that can compensate the velocity-dependent time-of-flight difference accumulated during beam propagation. The first-order compression condition at the target position can be expressed as [36]

$$R_{56} = 2\rho \sin\alpha - 2\rho\alpha + \frac{L_z}{\gamma^2} \approx 0, \tag{3}$$

where ρ, α, L_z and γ denote the dipole bending radius, the bending angle, the effective propagation distance to the target position, and the relativistic Lorentz factor of the reference particle, respectively. The first two terms describe the geometrical path-length contribution introduced by the DBA, while the last term represents the

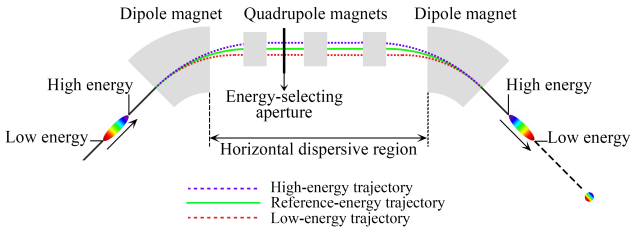


FIG. 1. Schematic of DBA-based compression.

velocity-dependent longitudinal dispersion accumulated during propagation.

In the first dipole, electrons with different energies acquire energy-dependent horizontal offsets in the dispersive region. An aperture placed in this region defines the transmitted energy window and provides a direct means of aperture-based phase-space control. Its transverse position determines the energy-window center, while its opening controls the transmitted energy spread. The intermediate quadrupole section provides transverse focusing and optical matching to establish the horizontal phase-space symmetry required for DBA transport, and the second dipole recombines the trajectories at the DBA exit. During subsequent propagation, higher-energy electrons travel slightly faster and catch up with lower-energy electrons, thereby realizing first-order temporal compression at the target position.

B. Simulation of Energy-Window-Dependent Nonlinear LPS Evolution

To establish the phase-space basis for aperture-based compression optimization, numerical simulations were performed to analyze the nonlinear LPS evolution through the DBA section and the dependence of the final bunch length on the energy-window condition. The simulation parameters were chosen to match the experimentally relevant LWFA-UED beam conditions, while the initial 6% full-width at half-maximum (FWHM) energy spread provides a sufficiently broad phase-space range for applying the narrower energy windows used in the following analysis. The simulations were performed with a bunch charge of 5 fC, a central energy of 4.55 MeV and an initial root-mean-square (RMS) bunch length of 10 fs, with space-charge effects included. Figure 2(a) shows the simulated LPS after drift-only propagation without the DBA. Although higher-order longitudinal dispersion is also present in a drift section, the velocity-dependent time-of-flight difference is dominated by the first-order term under this condition, leading to pronounced temporal elongation while the nonlinear curvature remains weak. With the DBA, the full-compression condition is considered first, where the first-order longitudinal dispersion R_{56} is reduced to near zero while second-order longitudinal transport remains appreciable, as shown in Fig. 2(c). For comparison, the under- and over-compression conditions are also considered, corresponding to positive and negative R_{56}, respectively, as shown in Figs. 2(e) and 2(g). Compared with the full compensated case, the nonzero first-order contributions in these two cases impose linear tilts of opposite signs on the nonlinear LPS and shift the low-slope region of the nonlinear LPS to different energy regions. For such a nonlinear LPS, the final temporal profile depends not only on the energy spread, but also on the position of the energy window within the LPS.

To quantify these effects, energy windows with different central energies and energy spreads were applied to the LPS distributions. The central energies were set to 4.53, 4.55, and 4.57 MeV to compare different positions within the LPS, corresponding to the low-energy side, the reference-energy region, and the high-energy side, respectively. The FWHM energy spreads were set to 2%, 3%, and 4% to examine the dependence of the RMS bunch length on the transmitted energy spread, as shown in Figs. 2(b), 2(d), 2(f), and 2(h).

The observed dependence can be interpreted using the local time–energy slope relation in Eq. (2). As the energy-window position changes, the transmitted electrons occupy different local-slope regions of the nonlinear LPS; as the transmitted energy spread increases, the window covers a broader nonlinear phase-space range. Although the simulations include space-charge effects and the realistic beam distribution, these effects remain moderate for the fC-level bunch charge considered here, so this transport picture provides a useful basis for identifying the dominant bunch-length dependence on the energy-window condition. The trends observed in Figs. 2(b), 2(d), 2(f), and 2(h) therefore reflect the combined influence of the local time–energy slope and the width of the transmitted energy window. The bunch length can be minimized when the transmitted energy window is aligned with a region of small local time–energy slope and the energy spread is sufficiently controlled. These results provide the phase-space criterion used below to interpret the experimentally measured LPS distributions and to optimize the aperture-defined energy-window condition.

III. THZ-TDC-BASED LPS DIAGNOSTICS

A. Experimental Setup and THz Pulse Characterization

The THz-TDC-based LPS diagnostic system was implemented on a compact LWFA-UED beamline, as shown in Fig. 3(a). The system is driven by a Ti:sapphire laser amplifier operating at a central wavelength of 800 nm and a repetition rate of 10 Hz. The output pulse is split by a beam splitter (BS), with approximately 40% of the energy directed to the LWFA branch. In this branch, the pulse is compressed to 24 fs (FWHM) in a vacuum compressor and focused by an off-axis parabolic (OAP)

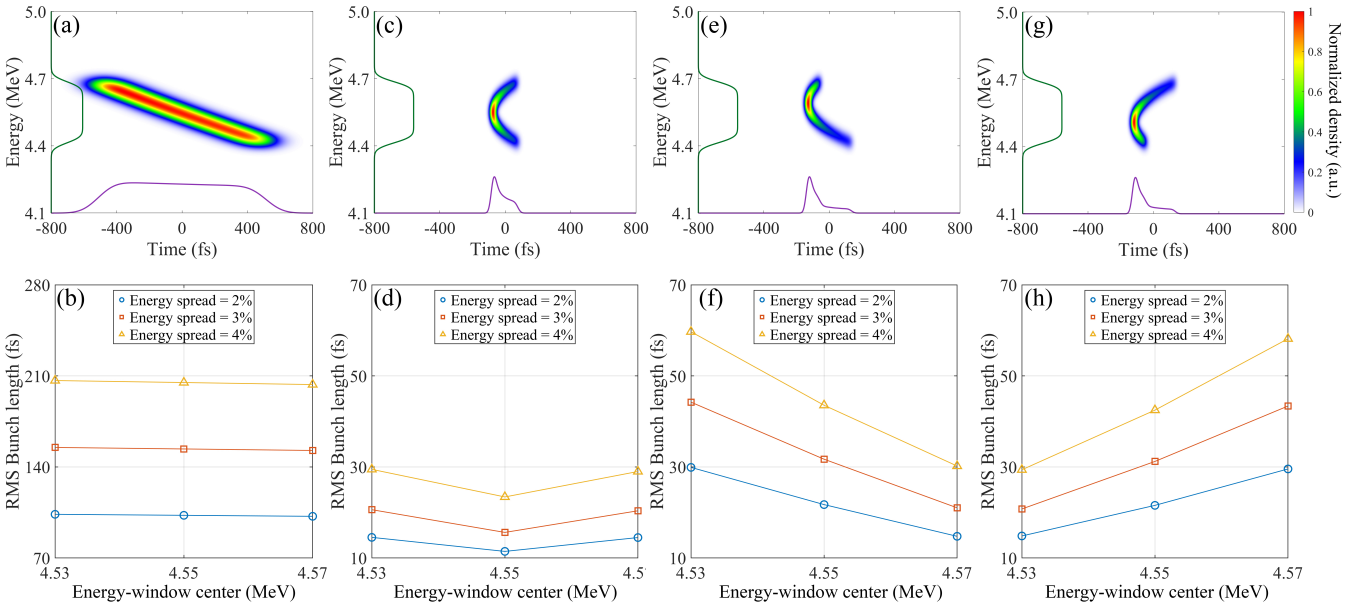


FIG. 2. Numerical simulations of LPS evolution and energy-window-dependent bunch length. The simulated LPS distributions and corresponding RMS bunch lengths are shown at the target plane under different transport conditions: (a,b) without the DBA, and with the DBA at (c,d) the full-compressed condition, (e,f) the under-compressed condition, and (g,h) the over-compressed condition with appreciable second-order longitudinal transport. In all LPS plots, the left side of the time axis corresponds to the bunch head.

mirror into a nitrogen gas target to generate relativistic electron bunches. The accelerated electrons are captured and focused by a quadrupole doublet, pass through the DBA section for aperture-defined energy-window control and longitudinal compression, and are subsequently transported to the THz-TDC interaction point for LPS characterization. The THz-TDC is based on a tapered rectangular waveguide fabricated in a split-block configuration, with the upper and lower halves machined separately and subsequently assembled.

The remaining $\sim$ 60% of the laser energy is directed to the THz generation branch. In this branch, the pulse is compressed by an independent compressor to a duration of approximately 400 fs (FWHM). To optimize high-field THz generation via optical rectification in a lithium niobate ($LiNbO_3$) crystal, the THz-generation pulse undergoes sequential energy and spectral conditioning, as shown in Fig. 3(a). The pulse energy is first continuously adjusted using a half-wave plate (HWP) and a thin-film polarizer (TFP), followed by a bandpass filter to narrow the spectrum and optimize phase-matching conditions.

Under an incident laser energy of $\sim$ 22 mJ, a single-pulse THz energy of $\sim$ 117 μJ was achieved at the source, corresponding to an optical rectification efficiency of approximately 0.53%. After transmission and focusing by an OAP with a hole, the THz pulse energy at the interaction point was measured to be $\sim$ 63 μJ. The THz temporal waveform measured via electro-optic sampling (EOS) and the corresponding frequency spectrum are shown in Fig. 3(b). The THz focal spot at the electron–THz interaction point, with a beam waist radius of approximately 1 mm, is shown in Fig. 3(c). Based on these parameters, the peak THz electric field is estimated using [37]

$$E_{\mathrm{THz}} = \sqrt{\frac{1}{c\varepsilon_0}\frac{2W_{\mathrm{THz}}}{\tau A}}, \tag{4}$$

where W_{THz} is the THz pulse energy, τ is the pulse duration, and A is the focal spot area. The peak THz electric field is thereby estimated to be approximately 137 MV/m, providing sufficient streaking strength for femtosecond-scale temporal diagnostics.

B. Temporal and Energy Resolutions

Before reconstructing the LPS, the temporal and energy resolutions were calibrated separately. For the temporal axis, the THz-TDC maps the longitudinal temporal coordinate of the electron bunch onto the vertical transverse coordinate through THz streaking. The temporal resolving power is determined by the unstreaked vertical beam size and the calibrated streaking strength. For the energy axis, the THz field is turned off, and the downstream dipole magnet maps the energy deviation onto the horizontal transverse coordinate. The energy resolution is determined by the intrinsic horizontal beam size and the horizontal dispersion at the detector plane.

The streaking strength was calibrated by scanning the relative delay between the THz pulse and the electron bunch, as shown in Fig. 4. Near the zero-crossing of

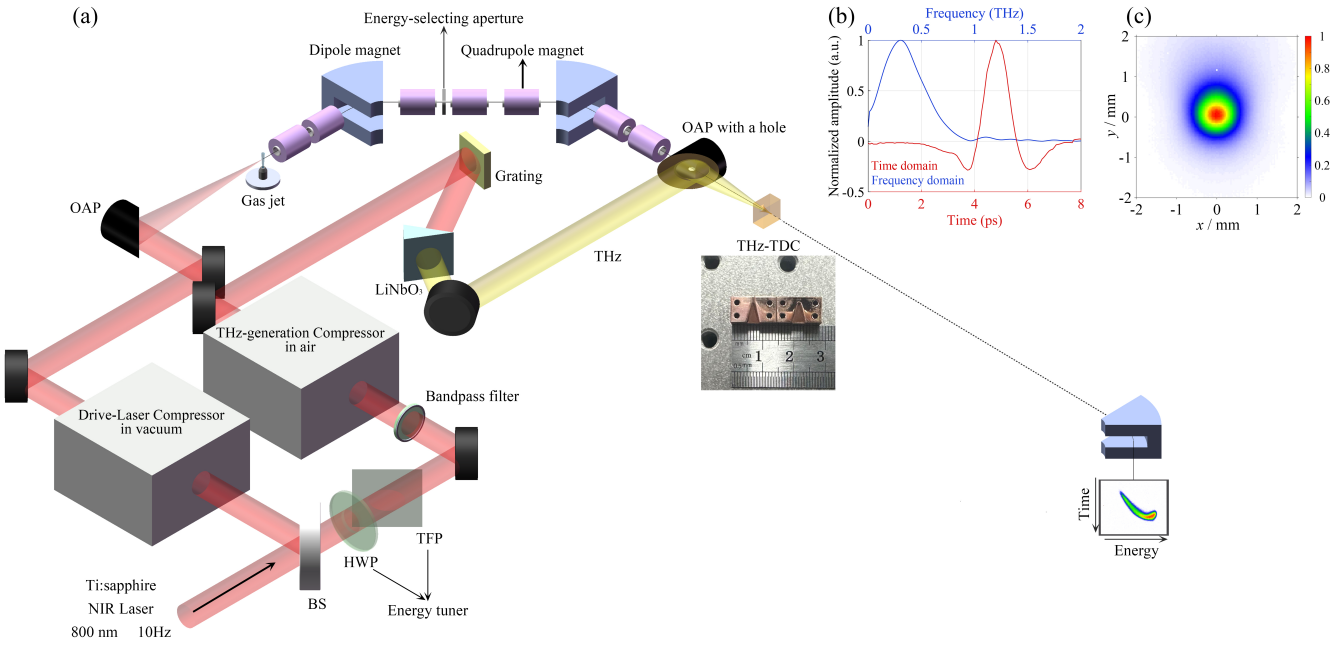


FIG. 3. Experimental setup and THz pulse characterization. (a) Layout of the LWFA-UED beamline and THz-TDC diagnostics. (b) THz temporal waveform (red) and corresponding frequency spectrum (blue). (c) Measured THz focal spot at the electron–THz interaction point.

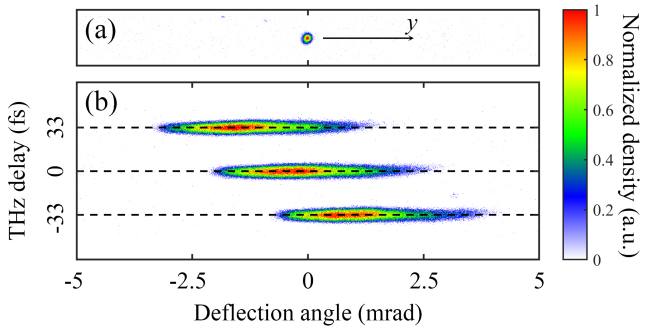


FIG. 4. THz-TDC streaking calibration. (a) Unstreaked electron beam spot. (b) Streaked beam spot and calibration of the streaking strength.

the THz field, the beam centroid varies linearly with the delay, yielding a calibrated streaking strength of $K \approx 36.2$ µrad/fs. Given a drift distance of $L_d \approx 2.97$ m from the THz-TDC to the imaging screen, the temporal resolution r_t is given by [25, 38]

$$r_t = \frac{\sigma_{y_0}}{K L_d}, \tag{5}$$

where σ_{y_0} is the unstreaked RMS vertical beam size. With $\sigma_{y_0} = 193 \pm 21$ µm, r_t is estimated to be 1.8 fs, with an uncertainty of approximately 0.2 fs mainly arising from fluctuations in the vertical beam size.

The energy resolution r_E is expressed as [28]

$$r_E = E_0 \frac{\sigma_{x_0}}{D_x}, \tag{6}$$

where E_0 is the average beam energy, D_x is the horizontal dispersion at the detector plane, and σ_{x_0} is the unstreaked horizontal RMS beam size. Using $E_0 = 4.55$ MeV, $D_x \approx 1.50$ mm/%, and $\sigma_{x_0} = 198 \pm 29$ µm, the energy resolution is estimated to be 6.0 keV, corresponding to a relative resolution of 0.13%. The uncertainty of this estimate, mainly arising from fluctuations in the horizontal beam size, is approximately 0.9 keV, corresponding to a relative uncertainty of 0.02%.

These calibrated resolutions are sufficient to resolve the femtosecond-scale temporal structure and the MeV-scale energy correlation of the compressed LWFA electron bunches.

C. LPS-Resolved Energy-Window Optimization

To use the measured nonlinear LPS as a guide for aperture-based compression optimization, LPS reconstruction was performed under different energy-window conditions using the calibrated THz-TDC diagnostic system. The aperture position and opening in the dispersive region controlled the central energy and energy spread, respectively. Each measurement therefore represents the LPS of electrons transmitted through a finite energy window. By scanning the aperture position and opening, different portions of the nonlinear time–energy correlation can be measured, and the full-energy-range LPS can in principle be reconstructed by combining these window-resolved LPS measurements. The following analysis therefore focuses on how the central

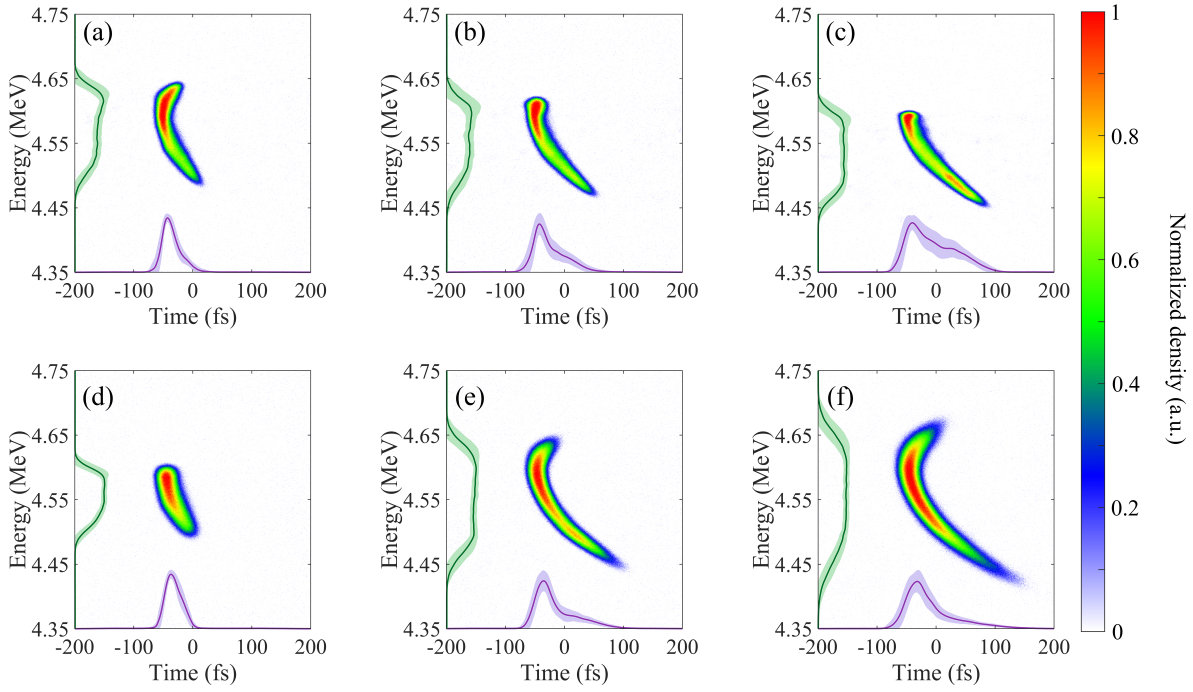


FIG. 5. Measured LPS distributions under aperture-defined energy-window conditions. Panels (a)–(c) show measurements with comparable FWHM energy spreads of approximately 2.8%–2.9% at central energies of 4.574 MeV (a), 4.554 MeV (b), and 4.532 MeV (c), respectively, illustrating the effect of energy-window position. Panels (d)–(f) show measurements near 4.55 MeV with FWHM energy spreads of 2.0% (d), 3.8% (e), and 4.4% (f), respectively, illustrating the effect of transmitted energy spread. The color maps show the reconstructed LPS density, with the green and purple marginal profiles denoting the energy and temporal projections, respectively. The shaded regions indicate the shot-to-shot standard deviation over 200 consecutive shots.

TABLE I. Energy-window conditions and measured RMS bunch lengths.

Case	Central energy	Energy spread (FWHM)	Bunch length (RMS)
a	4.574 ± 0.007 MeV	$2.9 \pm 0.3\%$	26 ± 3 fs
b	4.554 ± 0.009 MeV	$2.8 \pm 0.5\%$	35 ± 5 fs
c	4.532 ± 0.008 MeV	$2.9 \pm 0.4\%$	42 ± 5 fs
d	4.553 ± 0.005 MeV	$2.0 \pm 0.2\%$	27 ± 3 fs
e	4.552 ± 0.010 MeV	$3.8 \pm 0.4\%$	40 ± 4 fs
f	4.552 ± 0.012 MeV	$4.4 \pm 0.6\%$	44 ± 6 fs

energy and energy spread of the transmitted window determine the temporal projection of the bunch. Owing to the limited experimental space, the THz-TDC was positioned slightly downstream of the designed full-compensation point, so the measurements correspond to an under-compressed state with appreciable second-order longitudinal transport. In this state, the low-slope region around the LPS inflection point is shifted toward the high-energy side. The measured LPS distributions under different energy-window conditions are shown in Fig. 5. The corresponding energy-window conditions and measured RMS bunch lengths are summarized in Table I.

The role of energy-window position was first examined by shifting the central energy while maintaining a comparable energy spread of approximately 2.8%–2.9%. Consistent with this picture, the measured C-shaped LPS shows that the energy window centered at 4.574 ± 0.007 MeV covers a region with a smaller local time–energy slope, whereas shifting the window toward 4.532 ± 0.008 MeV selects a region with a larger slope. Correspondingly, the RMS bunch length increases from 26 ± 3 fs to 42 ± 5 fs. This trend shows that the aperture position controls the local time–energy slope covered by the transmitted electrons.

The influence of transmitted energy spread was then examined with the central energy kept near the reference-particle energy of 4.55 MeV. As summarized in Table I, the RMS bunch length shows an overall increasing trend from 27 ± 3 fs to 44 ± 6 fs as the FWHM energy spread increases from $2.0 \pm 0.2\%$ to $4.4 \pm 0.6\%$. Although adjacent cases partially overlap within their uncertainties, the trend indicates that increasing the aperture opening

includes a broader portion of the nonlinear LPS in the temporal projection, leading to a longer bunch duration.

These measurements show that the reconstructed nonlinear LPS can serve as an optimization map for DBA-compressed LWFA beams. The aperture position determines the local time–energy slope covered by the transmitted electrons, while the aperture opening determines the range of nonlinear phase space included in the temporal projection. Therefore, optimized compression requires both aligning the transmitted energy window with a small-slope region of the nonlinear LPS and maintaining an appropriate energy spread. This converts the LPS measurement from a diagnostic of nonlinear transport into a practical guide for aperture-based compression optimization in LWFA-UED beamlines.

IV. CONCLUSION

In summary, an integrated diagnostic system based on a THz-TDC and a dipole magnet has been implemented for two-dimensional LPS reconstruction of LWFA electron bunches during DBA-based compression. For electron bunches with an average energy around 4.55 MeV, the diagnostic system achieves a temporal resolving power of 1.8 fs and an energy resolution of 6.0 keV, corresponding to a relative energy resolution of 0.13%. The system directly resolves a characteristic C-shaped LPS induced by higher-order longitudinal transport, providing direct experimental access to the nonlinear time–energy correlation that limits the final bunch duration. The measured LPS shows that optimized DBA compression requires simultaneous matching of the beam central energy, the first-order longitudinal dispersion compensation, and the energy spread. The first-order dispersion R_{56} determines the main compression condition and the local time–energy slope near the beam center, while the second-order term T_{566} introduces nonlinear curvature that can broaden the temporal projection even when the first-order elongation is nearly compensated. Therefore, short-bunch operation requires the beam to be centered in a low-slope region of the nonlinear LPS, with the energy spread sufficiently controlled to avoid excessive sampling of the curved phase-space region.

Beyond identifying the optimal operating condition in the present experiment, the LPS measurement provides direct guidance for DBA beamline design. It can be used to evaluate whether the designed first-order dispersion compensation matches the actual beam central energy, to determine the acceptable energy-spread range, and to assess the need for higher-order longitudinal correction. In particular, the measured C-shaped LPS provides an experimental basis for future T_{566} compensation or linearization, for example by introducing sextupole magnets in the dispersive section [29]. Such LPS-guided matching of first- and second-order longitudinal transport could further improve bunch compression and support the development of LWFA-UED toward sub-10 fs temporal resolution.

ACKNOWLEDGMENTS

The authors would like to acknowledge Dr. Xiaonan Ning and Dr. Jiucheng Chen for their valuable assistance in optimizing the laser system; Dr. Wentao Yu and Kai Peng for their assistance with the setup of the THz system; and Dr. Yuemei Tan and Peng Lv for helpful discussions on the THz-TDC. The authors also gratefully acknowledge financial support from the Strategic Priority Research Program of the Chinese Academy of Sciences (Grant No. XDB0530000), Beijing Natural Science Foundation (Grant No. L2602047), the National Natural Science Foundation of China (Grant No. 12405169) and the Discipline Construction Foundation of the "Double World-Class Project". The numerical simulations were carried out using the computational resources provided by the High Performance Computing Center of Tsinghua University.

[1] B. J. Siwick, J. R. Dwyer, R. E. Jordan, and R. D. Miller, An atomic-level view of melting using femtosecond electron diffraction, Science **302**, 1382 (2003).

[2] M. Mo, Z. Chen, R. Li, M. Dunning, B. Witte, J. Baldwin, L. Fletcher, J. Kim, A. Ng, R. Redmer, *et al.*, Heterogeneous to homogeneous melting transition visualized with ultrafast electron diffraction, Science **360**, 1451 (2018).

[3] J. Yang, X. Zhu, T. J. Wolf, Z. Li, J. P. F. Nunes, R. Coffee, J. P. Cryan, M. Gühr, K. Hegazy, T. F. Heinz, *et al.*, Imaging CF_3I conical intersection and photodissociation dynamics with ultrafast electron diffraction, Science **361**, 64 (2018).

[4] J. Yang, X. Zhu, J. P. F. Nunes, J. K. Yu, R. M. Parrish, T. J. Wolf, M. Centurion, M. Gühr, R. Li, Y. Liu, *et al.*, Simultaneous observation of nuclear and electronic dynamics by ultrafast electron diffraction, Science **368**, 885 (2020).

[5] R. Li and P. Musumeci, Single-shot MeV transmission electron microscopy with picosecond temporal resolution, Physical Review Applied **2**, 024003 (2014).

[6] M. Kuwahara and T. Agemura, Temporal resolution in transmission electron microscopy using a photoemission electron source, Microscopy **72**, 97 (2023).

[7] C. Zhang, J. Hua, Y. Wan, C.-H. Pai, B. Guo, J. Zhang, Y. Ma, F. Li, Y. Wu, H.-H. Chu, *et al.*, Femtosecond probing of plasma wakefields and observation of the plasma wake reversal using a relativistic electron bunch, Physical Review Letters **119**, 064801 (2017).

[8] Y. Wan, S. Tata, O. Seemann, E. Y. Levine, E. Kroupp, and V. Malka, Real-time visualization of the laser-plasma wakefield dynamics, Science advances **10**, eadj3595

(2024).
[9] A. Khachatryan, A. Irman, F. Van Goor, and K.-J. Boller, Femtosecond electron-bunch dynamics in laser wakefields and vacuum, Physical Review Special Topics—Accelerators and Beams **10**, 121301 (2007).
[10] D. Papp, N. Hafz, and C. Kamperidis, Self-induced ionization injection LWFA and generation of sub-fs electron bunches with few-cycle sub-TW laser pulses, Laser and Particle Beams **37**, 165 (2019).
[11] P. Winkler, M. Trunk, L. Hübner, A. Martinez de la Ossa, S. Jalas, M. Kirchen, I. Agapov, S. Antipov, R. Brinkmann, T. Eichner, *et al.*, Active energy compression of a laser-plasma electron beam, Nature **640**, 907 (2025).
[12] E. Esarey, C. B. Schroeder, and W. P. Leemans, Physics of laser-driven plasma-based electron accelerators, Reviews of Modern Physics **81**, 1229 (2009).
[13] A. Pak, K. Marsh, S. Martins, W. Lu, W. Mori, and C. Joshi, Injection and trapping of tunnel-ionized electrons into laser-produced wakes, Physical Review Letters **104**, 025003 (2010).
[14] J. Zhu, R. Assmann, M. Dohlus, U. Dorda, and B. Marchetti, Sub-fs electron bunch generation with sub-10-fs bunch arrival-time jitter via bunch slicing in a magnetic chicane, Physical Review Accelerators and Beams **19**, 054401 (2016).
[15] A. He, F. Willeke, L. Yu, L. Yang, T. Shaftan, G. Wang, Y. Li, Y. Hidaka, and J. Qiang, Design of low energy bunch compressors with space charge effects, Physical Review Special Topics-Accelerators and Beams **18**, 014201 (2015).
[16] T. LT, Types of magnetic compressors the compres, Accelerator Physics and Engineering , 334.
[17] H. A. Enge, Achromatic magnetic mirror for ion beams, Review of Scientific Instruments **34**, 385 (1963).
[18] A. Rajabi, J. Jazini, M. Fathi, M. Sharifian, and B. Shokri, Design, construction and measurements of an alpha magnet as a solution for compact bunch compressor for the electron beam from thermionic RF Gun, Journal of Instrumentation **13** (03), T03002.
[19] Y. Yang, Z. Wang, P. Lv, B. Song, P. Huang, Y. Jia, Z. Liu, L. Zheng, W. Huang, P. Musumeci, *et al.*, Sub-5-fs compression and synchronization of relativistic electron bunches enabled by a high-gradient α-magnet and low-jitter photoinjector, arXiv preprint arXiv:2508.03946 (2025).
[20] A. Pires, V. Le Flanchec, A.-S. Chauchat, and N. Delerue, Comparison of the simulation of electron beam transport in the double alpha magnet compressor of a 17-MeV electron accelerator using CST PS, TraceWin, and RF-Track, Nuclear Instruments and Methods in Physics Research Section A: Accelerators, Spectrometers, Detectors and Associated Equipment **1077**, 170541 (2025).
[21] Y. Fang, F. Li, J. Hua, B. Guo, L. Zhou, B. Zhou, Z. Chen, J. Liu, Z. Zhou, Y. Wu, *et al.*, Ultrafast electron diffraction with MeV electron source from a laser wakefield accelerator, arXiv preprint arXiv:2210.12093 (2022).
[22] H. W. Kim, N. A. Vinokurov, I. H. Baek, K. Y. Oang, M. H. Kim, Y. C. Kim, K.-H. Jang, K. Lee, S. H. Park, S. Park, *et al.*, Towards jitter-free ultrafast electron diffraction technology, Nature Photonics **14**, 245 (2020).
[23] F. Qi, Z. Ma, L. Zhao, Y. Cheng, W. Jiang, C. Lu, T. Jiang, D. Qian, Z. Wang, W. Zhang, *et al.*, Breaking 50 femtosecond resolution barrier in MeV ultrafast electron diffraction with a double bend achromat compressor, Physical Review Letters **124**, 134803 (2020).
[24] P. Emma, J. Frisch, and P. Krejcik, A transverse RF deflecting structure for bunch length and phase space diagnostics, LCLS Technical Note **12** (2000).
[25] D. Marx, R. Assmann, P. Craievich, U. Dorda, A. Grudiev, and B. Marchetti, Longitudinal phase space reconstruction simulation studies using a novel X-band transverse deflecting structure at the SINBAD facility at DESY, Nuclear Instruments and Methods in Physics Research Section A: Accelerators, Spectrometers, Detectors and Associated Equipment **909**, 374 (2018).
[26] H. Loos, P. Bolton, J. Clendenin, D. Dowell, S. Gierman, C. Limborg, J. Schmerge, T. Shaftan, and B. Sheehy, Longitudinal phase space tomography at the SLAC gun test facility and the BNL DUV-FEL, Nuclear Instruments and Methods in Physics Research Section A: Accelerators, Spectrometers, Detectors and Associated Equipment **528**, 189 (2004).
[27] D. Malyutin, M. Gross, I. Isaev, M. Khojoyan, G. Kourkafas, M. Krasilnikov, B. Marchetti, M. Otevrel, F. Stephan, and G. Vashchenko, Longitudinal phase space tomography using a booster cavity at PITZ, Nuclear Instruments and Methods in Physics Research Section A: Accelerators, Spectrometers, Detectors and Associated Equipment **871**, 105 (2017).
[28] P. Dijkstal, W. Qin, and S. Tomin, Longitudinal phase space diagnostics with a nonmovable corrugated passive wakefield streaker, Physical Review Accelerators and Beams **27**, 050702 (2024).
[29] R. England, J. Rosenzweig, G. Andonian, P. Musumeci, G. Travish, and R. Yoder, Sextupole correction of the longitudinal transport of relativistic beams in dispersionless translating sections, Physical Review Special Topics-Accelerators and Beams **8**, 012801 (2005).
[30] E. Vogel, C. Albrecht, N. Baboi, C. Behrens, T. Delfs, J. Eschke, C. Gerth, M. Hoffmann, M. Hoffmann, M. Hüning, *et al.*, Test and commissioning of the third harmonic RF system for FLASH, Proceedings of IPAC **10**, 4281 (2010).
[31] Y. Wu, J. Hua, Z. Zhou, J. Zhang, S. Liu, B. Peng, Y. Fang, X. Ning, Z. Nie, Q. Tian, *et al.*, Tunable plasma linearizer for compensation of nonlinear energy chirp, Physical Review Applied **16**, 024056 (2021).
[32] Y. Wu, Z. Zhou, Y. Du, J. Hua, W. Lu, W. B. Mori, and C. Joshi, Linearization of an electron beam's longitudinal phase space using a hollow-channel plasma, Physical Review Applied **19**, 064013 (2023).
[33] L. Zhao, Z. Wang, C. Lu, R. Wang, C. Hu, P. Wang, J. Qi, T. Jiang, S. Liu, Z. Ma, *et al.*, Terahertz streaking of few-femtosecond relativistic electron beams, Physical Review X **8**, 021061 (2018).
[34] R. Li, M. Hoffmann, E. Nanni, S. Glenzer, M. Kozina, A. Lindenberg, B. Ofori-Okai, A. Reid, X. Shen, S. Weathersby, *et al.*, Terahertz-based subfemtosecond metrology of relativistic electron beams, Physical Review Accelerators and Beams **22**, 012803 (2019).
[35] L. Zhao, H. Tang, C. Lu, T. Jiang, P. Zhu, L. Hu, W. Song, H. Wang, J. Qiu, C. Jing, *et al.*, Femtosecond relativistic electron beam with reduced timing jitter from THz driven beam compression, Physical Review Letters **124**, 054802 (2020).

[36] Y. Fang, *MeV Ultrafast Electron Diffraction Based on Laser Wakefield Acceleration*, Ph.D. thesis, Tsinghua University, Beijing, China (2022), in Chinese.

[37] L. Guiramand, J. Nkeck, X. Ropagnol, T. Ozaki, and F. Blanchard, Near-optimal intense and powerful terahertz source by optical rectification in lithium niobate crystal, Photonics Research **10**, 340 (2022).

[38] P. Arpaia, R. Corsini, A. Gilardi, A. Mostacci, L. Sabato, and K. N. Sjobak, Enhancing particle bunch-length measurements based on radio frequency deflector by the use of focusing elements, Scientific Reports **10**, 11457 (2020).